Elaboration of collisional–radiative models for flows related to planetary entries into the Earth and Mars atmospheres

Arnaud Bultel, Julien Annaloro

Elaboration of collisional–radiative models for flows related to planetary entries into the Earth and Mars atmospheres

Arnaud Bultel and Julien Annaloro

CORIA, UMR CNRS 6614, Université de Rouen, Site universitaire du Madrillet, BP 12, 76801 Saint-Etienne du Rouvray, France

E-mail: Arnaud.Bultel@coria.fr

Abstract

The most relevant way to predict the excited state number density in a nonequilibrium plasma is to elaborate a collisional–radiative (CR) model taking into account most of the collisional and radiative elementary processes. Three examples of such an elaboration are given in this paper in the case of various plasma flows related to planetary atmospheric entries. The case of theoretical determination of nitrogen atom ionization or recombination global rate coefficients under electron impact is addressed first. The global rate coefficient can be implemented in multidimensional computational fluid dynamics calculations. The case of relaxation after a shock front crossing a gas of N_2 molecules treated in the framework of the Rankine–Hugoniot assumptions is also studied. The vibrational and electronic specific CR model elaborated in this case allows one to understand how the plasma reaches equilibrium and to estimate the role of the radiative losses. These radiative losses play a significant role at low pressure in the third case studied. This case concerns CO_2 plasma jets inductively generated in high enthalpy wind tunnels used as ground test facilities. We focus our attention on the behaviour of CO and C_2 electronic excited states, the radiative signature of which can be particularly significant in this type of plasma. These three cases illustrate the elaboration of CR models and their coupling with balance equations.

1. Introduction

A spacecraft coming close to a planet or a planetary satellite can be gravitationally captured [1]. Under particular conditions, this capture leads to a free fall at high velocity compatible with a final landing. The order of magnitude of the velocity reached by the spacecraft during this free fall is $10\,\mathrm{km\,s^{-1}}$ and challenges the integrity of the spacecraft if the planet or the satellite is surrounded by an atmosphere [2]. In fact, the resulting atmospheric entry occurs with a velocity largely higher than the speed of sound, which induces a strong compression of the incident gas near the fuselage over a shock layer (SL), the thickness of which is several centimetres [3]. Figure 1 is a schematic view of the flow structure around the body. The order of magnitude of the temperatures reached in the shock layer is 10 000 K [4] and leads to the gas → plasma transition with a strong heat transfer to the wall [5]. Under these conditions, the fuselage can be dramatically destroyed if no thermal protection system (TPS) is used.

The sizing of this TPS, the material of which must be appropriately chosen, results from the different contributions to the heat transfer. Owing to the low characteristic time scales of the compression with respect to equilibration time scales, the flow in the SL is in thermal and chemical nonequilibrium [6]. The heat transfer at the wall can then be separated into three parts. The first part results from the relaxation to the wall of internal modes of energy storage such as translation or vibration driven by transport coefficients such as thermal conductivity [7]. The second part is due to the relaxation to the wall of dissociation energy released by adsorbed atoms

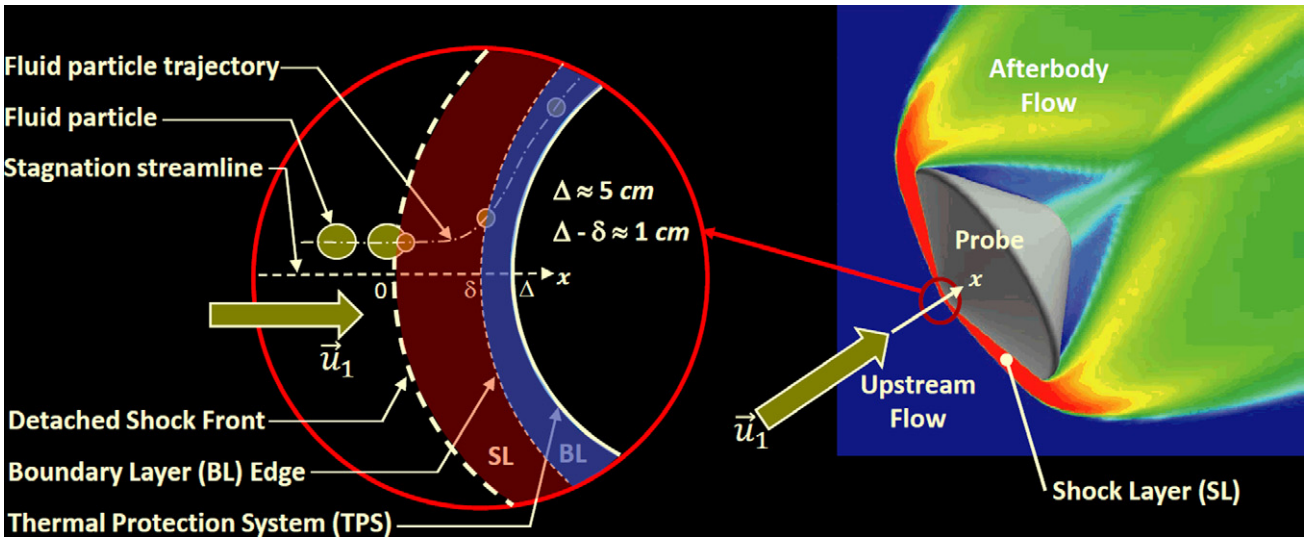

Figure 1. Schematic view of the flow around an incoming body. The structure of the flow along the stagnation streamline is detailed. A shock layer (SL) is formed between a detached shock front and the body surface over the thickness Δ (typically several centimetres). Inside the SL in the close vicinity of the body surface, a boundary layer (BL) is formed (thickness $\Delta - \delta$) corresponding to the energy release to the thermal protection system (TPS). Crossing the shock front, a fluid particle undergoes a strong compression leading to a significant increase in temperature.

recombining in molecules [8]. It is important to note that this part equals zero at equilibrium since the wall temperature ranges between 1000 and 2000 K for which the equilibrium dissociation degree of the concerned plasma is negligibly small. The third part results from the photons whose mean free path overcomes the SL thickness [9] and which are absorbed by the wall. These photons are produced by spontaneous emission from upper states of atomic and molecular excited species, the number density of which departs from equilibrium. This radiative contribution can be the most important part of the total heat flux [10].

Each previous contribution greatly depends on the excited state population densities and their distribution over the SL. A detailed description of their dynamics is therefore mandatory. In the past, global approaches have been developed for computational fluid dynamics (CFD) calculations of the flow. These approaches were based on the use of global (effective) rate coefficients treating the species as a whole, therefore by lumping all the states together. The resulting databases were implemented with specific routines allowing the calculation of the excited state number density with the help of relevant excitation temperatures [11]. Since the end of the last century, a renewed method of investigation has begun in order to reduce the number of assumptions on which previous works were based by considering detailed (state-to-state) chemistry and couplings with the Boltzmann equation [12, 13]. This approach requires a huge amount of elementary data and cannot be performed for every situation. In addition, in the case of two-dimensional flow field modelling, they lead to prohibitive calculation times and have not been successfully performed so far. Our contribution to this new method deals with the elaboration of collisional–radiative (CR) models, the purpose of which is to highlight the specific behaviour of excited states and the role they are playing in the chemistry. This work is based on the thorough treatment of the source term of the individual balance equations.

In this paper, three situations are studied from the simplest to the most complicated from the dimensional point of view. The first (0D) situation corresponds to the theoretical determination of global rate coefficients for atomic ionization or recombination resulting from the behaviour of the excited states for implementation in multidimensional CFD calculations. The concept of global rate coefficient is analysed. The second situation (1D) is described, in which a complete coupling with the flow is implemented in the case of the crossing of a shock front in pure N_2 in relation to entry in the Earth's atmosphere. The state-to-state approach developed in this case enables one to emphasize the time scales of energy storage in the different modes. The last situation (axisymmetric pseudo-2D) concerns CO_2 plasma jets produced with high enthalpy wind tunnels (HEWTs) used as ground test facilities to test TPS materials in the context of Mars atmospheric entries. The characteristic scales required for equilibrium, and the influence of radiation and transport on equilibrium, can then be estimated.

2. Case 0D: atomic CR model for ionization or recombination

2.1. Treatment of the balance equation

The balance equation for a species X in its excited state i is classically written in the form

$$\frac{\partial \rho_{X_i}}{\partial t} + \vec{\nabla} \cdot \left(\rho_{X_i} \vec{u} + \vec{J}_{X_i} \right) = \dot{\rho}_{X_i}, \qquad (1)$$

where ρ_{X_i} is the X_i mass density, $\vec{u}$ is the barycentric velocity, $\vec{J}_{X_i}$ is the diffusion mass flux density vector of X_i and $\dot{\rho}_{X_i}$ is the mass source term of X_i. This source term results from the collisional and radiative elementary processes and can be mathematically obtained as the sum $(\dot{\rho}_{X_i})_C + (\dot{\rho}_{X_i})_R$ whose terms are relative to each contribution.

Three characteristic time scales can be defined for the transport term of equation (1). The convective time scale is defined as

$$\tau_{\rm c} = \pm \frac{\rho_{X_i}}{\left(\vec{\nabla}\rho_{X_i}\right)\cdot\vec{u}}. \tag{2}$$

Expansion or contraction of the flow can lead to variations of the local density for X_i. The related time scale reads

$$\tau_{\rm ec} = \pm \frac{1}{\vec{\nabla}\cdot\vec{u}}. \tag{3}$$

The characteristic time scale for diffusion is given by

$$\tau_{\rm d} = \pm \frac{\rho_{X_i}}{\vec{\nabla}\cdot\vec{J}_{X_i}}. \tag{4}$$

In previous equations, the positive sign or the negative sign has to be used if the sign of the denominator is positive or negative, respectively.

Equation (1) is then modified. Noting $[X_i] = \rho_{X_i}/m_{X_i}$ the number density for which m_{X_i} is the particle mass, one obtains after some algebra

$$\frac{\partial[X_i]}{\partial t} \pm \frac{[X_i]}{\tau_{\rm c}} \pm \frac{[X_i]}{\tau_{\rm ec}} \pm \frac{[X_i]}{\tau_{\rm d}} = [\dot{X}_i]_{\rm C} + [\dot{X}_i]_{\rm R}. \tag{5}$$

In the case where the source term is dominant, number density gradients play a minor role ($\partial/\partial t \equiv {\rm d}/{\rm d}t$) and the characteristic time scale of the source term is largely shorter than $\tau_{\rm c}$ and $\tau_{\rm d}$. The asymptotic limit corresponds to a uniform system, therefore to the 0D case. Equation (5) is simplified under the form

$$\frac{{\rm d}[X_i]}{{\rm d}t} \pm \frac{[X_i]}{\tau_{\rm ec}} = [\dot{X}_i]_{\rm C} + [\dot{X}_i]_{\rm R}. \tag{6}$$

Considering a closed volume V without inner swirls, we have $\vec{\nabla}\cdot\vec{u} = \frac{1}{V}\frac{{\rm d}V}{{\rm d}t}$, which leads to

$$\frac{{\rm d}[X_i]}{{\rm d}t} + \frac{[X_i]}{V}\frac{{\rm d}V}{{\rm d}t} = [\dot{X}_i]_{\rm C} + [\dot{X}_i]_{\rm R}. \tag{7}$$

The number of particles X_i inside V is denoted N_{X_i}. Finally, the balance equation is

$$\frac{1}{V}\frac{{\rm d}N_{X_i}}{{\rm d}t} = [\dot{X}_i]_{\rm C} + [\dot{X}_i]_{\rm R}. \tag{8}$$

2.2. CR source term

The previous form of the balance equation is particularly appropriate for the theoretical determination of global rate coefficients. We illustrate this determination in the following. Such rate coefficients are used in multidimensional CFD calculations when a relevant prediction of the species considered as a whole is required. In plasmas formed during entries into Earth's or Mars' atmosphere, atoms such as C, N, O and Ar are produced. They can be ionized under electron impact and lead to modifications of the ionization degree. The excitation and ionization elementary processes have to be considered simultaneously insofar as collisions between atoms and electrons can also lead to electronic excitation and play a significant role in the global process of ionization.

Thus, each elementary collisional coupling with another excited state j of the atom

$$X_i + {\rm e}^- \rightleftarrows X_{j>i} + {\rm e}^- \tag{9}$$

and with another excited state l of the ion

$$X_i + {\rm e}^- \rightleftarrows X_l^+ + 2\,{\rm e}^- \tag{10}$$

allows the global ionization inside V if the initial electron density is less than the equilibrium value

$$n_{\rm e}^{\rm S} = K^{\rm S}\left(\sqrt{1 + \frac{p}{K^{\rm S}\,k_{\rm B}\,T_{\rm e}}} - 1\right) \tag{11}$$

given by pressure p and electron temperature $T_{\rm e}$ initially chosen. Ionic excitation processes are also included. In the previous equation, $K^{\rm S}$ is the Saha equilibrium constant.

The backward elementary processes of deexcitation and recombination in (9) and (10) involve the following writing of the collisional source term of equation (8):

$$\begin{aligned}[\dot{X}_i]_{\rm C} = & -\sum_{j>i} k_{i\to j}\left(1 - \frac{[X_j]}{[X_i]\,K^B_{j,i}}\right)[X_i]\,n_{\rm e} \\ & + \sum_{j<i} k_{j\to i}\left(1 - \frac{[X_i]}{[X_j]\,K^B_{i,j}}\right)[X_j]\,n_{\rm e} \\ & - \sum_{i} k_{i\to l}\left(1 - \frac{[X_l^+]\,n_{\rm e}}{[X_i]\,K^S_{l,i}}\right)[X_i]\,n_{\rm e}\end{aligned} \tag{12}$$

using the concept of detailed balance totally relevant from the elementary point of view. $K^{\rm B}_{i,j}$ (and $K^{\rm B}_{j,i}$) and $K^{\rm S}_{l,i}$ are the elementary Boltzmann and Saha equilibrium constants, respectively. $n_{\rm e}$ is the electron density. The elementary rate coefficients $k_{i\to j}$ and $k_{j\to i}$ refer to excitation and $k_{i\to l}$ is related to ionization.

In many situations, the collision frequency is sufficiently high and the radiative source term $[\dot{X}_i]_{\rm R}$ is negligibly small in equation (8). The species variation rate, therefore purely collisional, is then deduced from

$$\frac{1}{V}\frac{{\rm d}N_X}{{\rm d}t} = \sum_i \frac{1}{V}\frac{{\rm d}N_{X_i}}{{\rm d}t} = \sum_i [\dot{X}_i]_{\rm C} \tag{13}$$

for the neutrals and from

$$\frac{1}{V}\frac{{\rm d}N_{X^+}}{{\rm d}t} = \sum_l \frac{1}{V}\frac{{\rm d}N_{X_l^+}}{{\rm d}t} = \sum_l [\dot{X}_l^+]_{\rm C} \tag{14}$$

for the ions inside V.

2.3. Excited state dynamics and global rate coefficient

We have used the same well-known cross section set due to Drawin [14] to calculate the elementary rate coefficients $k_{i\to j}$, $k_{j\to i}$ and $k_{i\to l}$ of equation (12) in a unified approach for $X \equiv$ C, N, O and Ar (see table 1). The energy diagram of these atoms is taken from the NIST database [15] and is summarized in table 2.

Table 1. Rate coefficients for elementary processes of excitation and ionization used in section 2.3 and based on cross sections given by Drawin [14].

Elementary process	Transition type	Rate coefficient
$X_i + e^- \rightarrow X_{j>i} + e^-$	Allowed	$\bar{v}_e\, 4\pi a_0^2\, a^2\, \alpha^A\, (\frac{E_{ion}^H}{E_j - E_i})^2\, I_2(a, \beta^A)$ with $\bar{v}_e = \sqrt{\frac{8\, k_B\, T_e}{\pi\, m_e}}$, $a = \frac{E_j - E_i}{k_B\, T_e}$, a_0 is the first Bohr radius, $\alpha^A = 1$, E_{ion}^H is the ionization energy of hydrogen atom, $I_2(a, \beta^A) = I_1(a) \ln(\frac{5}{4}\beta^A) + \frac{\mathcal{E}_1(a)}{a} - G_2(a)$, $\beta^A = 1$, $\mathcal{E}_1(a)$ order 1 exponential integral, $G_2(a)$ order 2 generalized exponential integral.
$X_i + e^- \rightarrow X_{j>i} + e^-$	Parity forbidden	$\bar{v}_e\, 4\pi a_0^2\, a^2\, \alpha^P\, I_1(a)$ with $\alpha^P = 0.05$, $I_1(a) = \frac{e^{-a}}{a} - \mathcal{E}_1(a)$.
$X_i + e^- \rightarrow X_{j>i} + e^-$	Spin forbidden	$\bar{v}_e\, 4\pi a_0^2\, a^2\, \alpha^S\, I_3(a)$ with $\alpha^S = 0.1$, $I_3(a) = \mathcal{E}_2(a) - \mathcal{E}_4(a)$, $\mathcal{E}_2(a)$ order 2 exponential integral, $\mathcal{E}_4(a)$ order 4 exponential integral.
$X_i + e^- \rightarrow X_l^+ + e^-$	Allowed	$\bar{v}_e\, 4\pi a_0^2\, a^2\, \alpha^+\, (\frac{E_{ion}^H}{E_n - E_m})^2\, I_2(a, \beta^+)$ with $\alpha^+ = 0.67$, $\beta^+ = 1$.

Table 2. Energy diagram of C, N, O and Ar used in section 2.3 [15].

Atom	Ground state	Excited states	Number of atomic states	Ground ionic state	Number of ionic states
C	$^3P_0$	$^3P_1$, $^3P_2$, $^1D_2$, ...	265	$^2P^o_{1/2}$	8
N	$^4S^o_{3/2}$	$^2D^o_{5/2}$, $^2D^o_{3/2}$, $^2P^o_{1/2}$, ...	251	$^3P_0$	9
O	$^3P_2$	$^3P_1$, $^3P_0$, $^1D_2$, ...	127	$^4S^o_{3/2}$	8
Ar	$^1S_0$	$^2[\frac{3}{2}]^o_2$, $^2[\frac{1}{2}]^o_0$, $^2[\frac{3}{2}]^o_1$, ...	379	$^2P^o_{3/2}$	7

Drawin's cross sections lack accuracy with respect to experimental cross sections for transitions between low-lying levels. However, we preferred to work with them because they form a self-consistent set which can be used for C, N, O and Ar. In addition, their accuracy is satisfactory from the order of magnitude point of view as illustrated by the comparison of the global three-body recombination rate coefficient calculated with them [16] and with experimental cross sections [17] (discrepancy less than 30% over the range $4500\,\mathrm{K} < T_e < 8300\,\mathrm{K}$ for argon). Moreover, the direct influence of the energy diagram can be easily studied. We have shown that lumping the levels over an energy width ΔE_l of the order of the thermal energy quantum $k_B T_A$ does not change the results greatly. Such a procedure is therefore used in section 3.2. Using Drawin's cross sections whatever the species remains a stopgap solution. Over the last two decades, the HULLAC package (in part based on the distorted wave approximation) has been elaborated [28]. Its intensive use will shortly provide the required cross sections which will be implemented instead of those due to Drawin after systematic comparisons with available experimental data. This work is in progress.

Figure 2 illustrates the time evolution of representative states of N under the typical entry conditions $p = 10\,000\,\mathrm{Pa}$ and $T_e = 10\,000\,\mathrm{K}$ in an ionization situation ($n_e(t = 0) = 10^{10}\,\mathrm{m^{-3}} < n_e^S \simeq 5 \times 10^{21}\,\mathrm{m^{-3}}$). The calculation is performed without coupling with energy balance, therefore by keeping constant pressure and electron temperature. Three successive phases can be observed. First, the excited states relax owing to the initial conditions ($0 < t < \tau_{QSS} \simeq 2 \times 10^{-6}$ s). Then, the excited states reach a quasi-steady state (QSS) corresponding to lower densities with respect to equilibrium. During this second phase, electron density (equal to the N^+ density by virtue of electroneutrality) increases until n_e reaches a value close to n_e^S. The recombination elementary processes begin to play a significant role which leads to an increase in the excited state number density and to a decrease in the ground state density. In fact, the total density does not evolve since pressure and electron temperature are taken constant. The third phase is then reached at time $t \simeq 2 \times 10^{-5}$ s and densities are constant. This phase corresponds to equilibrium since the source term $[\dot{X}_i]_R$ has been neglected in the present case.

Figure 2 clearly shows that a dynamical coupling takes place during the QSS. Each excited level i is populated by excitation from lower levels and depopulated by excitation to more excited levels or by direct ionization. The total rate of the populating elementary processes counterbalances rigorously the total rate of the depopulating elementary processes which leads to a net rate close to 0 for each excited level i. As a result, the excited state number density temporary stabilizes. This leads to a particular distribution of the excited state population

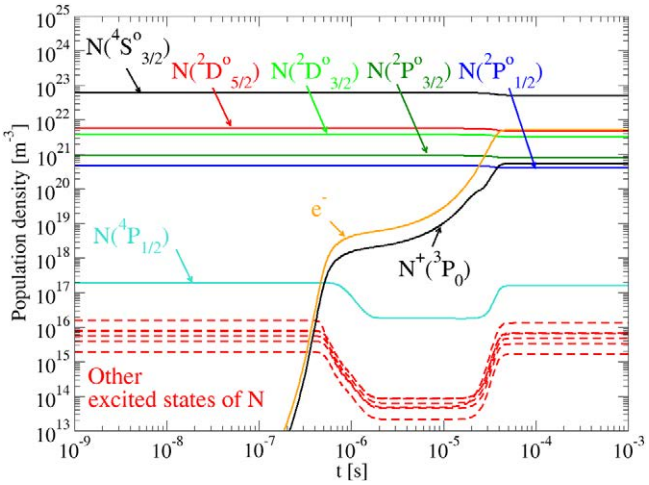

Figure 2. Time evolution of the population density of the ground state ($^4S^o_{3/2}$), metastable states ($^2D^o_{5/2}$, $^2D^o_{3/2}$, $^2P^o_{1/2}$, and $^2P^o_{3/2}$ in order of increasing energy), and other excited states of nitrogen for an ionization configuration at $T_e = 10\,000$ K and $p = 10\,000$ Pa. The initial excitation temperature is $T_{exc} = 10\,000$ K and the initial electron density is 10^{10} m^{-3}. p and T_e are constant. The three successive phases described in section 2.3 are observed: (1) relaxation $0 < t < \tau_{QSS} \simeq 2 \times 10^{-6}$ s, (2) quasi-steady state $\tau_{QSS} < t \lesssim 2 \times 10^{-5}$ s, (3) final equilibrium state $t \gtrsim 2 \times 10^{-5}$ s. For clarity, only the ground state $^3P_0$ of N^+ is shown.

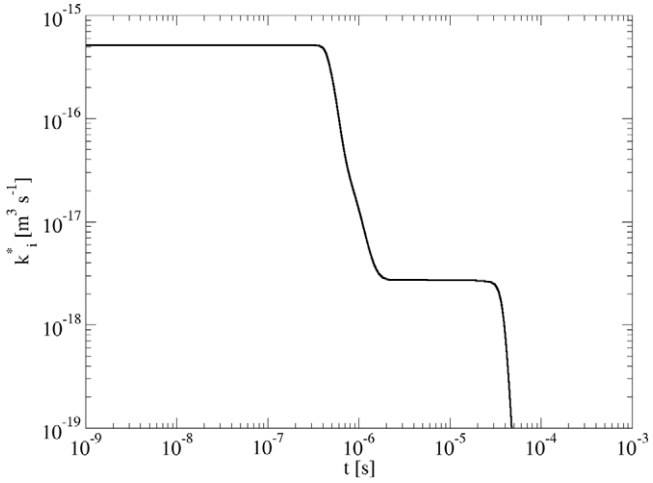

Figure 3. Time evolution of parameter k_i^* defined by equation (15) for the conditions $T_e = 10\,000$ K and $p = 10\,000$ Pa for N. The initial conditions ($n_e(t = 0) = 10^{10}$ m^{-3}, $T_{exc}(t = 0) = 10\,000$ K) correspond to figure 2. The three successive phases already seen in figure 2 are observed. In particular, the QSS characterized by $\partial k_i^*/\partial t = 0$ is obvious near 10^{-5} s.

density, and therefore to the aforementioned coupling. This coupling depends neither on the initial conditions nor on the pressure. It is particularly well displayed by the parameter

$$k_i^*(t) = -\frac{1}{[N]\,n_e}\left(\frac{d[N]}{dt} + \frac{[N]}{V}\frac{dV}{dt}\right), \qquad (15)$$

the time evolution of which is illustrated by figure 3. The QSS corresponds to the plateau of k_i^* at a value depending on T_e only. Under the present conditions, we have $k_{i,QSS}^* = 2.8 \times 10^{-18}$ m^3 s^{-1}.

The global rate coefficient of nitrogen ionization is defined as the steady T_e-dependent parameter k_i that links the species variation rate and the densities by the classical differential equation

$$\frac{1}{V}\frac{dN_{N^+}}{dt} = \frac{1}{V}\frac{dN_e}{dt} = -\frac{1}{V}\frac{dN_N}{dt} = k_i\,[N]\,n_e. \qquad (16)$$

From this equation, we deduce

$$k_i = -\frac{1}{[N]\,n_e}\left(\frac{d[N]}{dt} + \frac{[N]}{V}\frac{dV}{dt}\right). \qquad (17)$$

Since k_i is time-independent, the comparison between equations (15) and (17) leads to identifying k_i with $k_{i,QSS}^*$. The global rate coefficient is therefore determined.

We have used the previous procedure over the range $3000\,\text{K} < T_e < 20\,000\,\text{K}$ and determined the global rate coefficient, the evolution of which is displayed in figure 4. This evolution is compatible with the modified (three-parameter) Arrhenius law

$$k_i = 32\,T_e^{-2.856}\,e^{-168\,970/T_e}\ \text{m}^3\,\text{s}^{-1}, \qquad (18)$$

which can be easily used in CFD calculations. In the rate coefficient (18), temperatures are expressed in K. Note that the activation temperature 168 970 K in the exponential term is close to E_{ioni}/k_B where E_{ioni} is the ionization limit of N (14.534 13 eV) and k_B is the Boltzmann constant.

Figure 4 also displays the literature reference data [18–23] for comparison. Our results correspond to high values within the range given by the literature. Since atomic nitrogen cannot be easily obtained experimentally under conditions appropriate to its thermal ionization by electron collisions, recombination experiments are performed instead. Many authors assume the detailed balance fulfilled for the global rate coefficients by writing

$$\frac{k_i}{k_r} = K^S, \qquad (19)$$

where the global rate coefficient for recombination is denoted k_r. k_i is then deduced from that related to recombination. The comparison between our results and those of the literature are therefore indirect and includes uncertainties resulting from the calculation of K^S. Consequently, a more valuable comparison between recombination rate coefficients has to be performed directly.

Our approach can also be used for recombination. Such a recombination situation can be easily obtained by assuming an initial value for n_e higher than the equilibrium value given by equation (11) resulting from the chosen p and T_e values. It is then possible to compare directly global rate coefficients with experimental results.

During a recombination situation, the excited states present a behaviour similar to that illustrated previously for ionization. Instead of being underpopulated with respect to equilibrium during the QSS, the excited states are overpopulated. The transient parameter

$$k_r^*(t) = -\frac{1}{[N^+]\,n_e^2}\left(\frac{d[N^+]}{dt} + \frac{[N^+]}{V}\frac{dV}{dt}\right) \qquad (20)$$

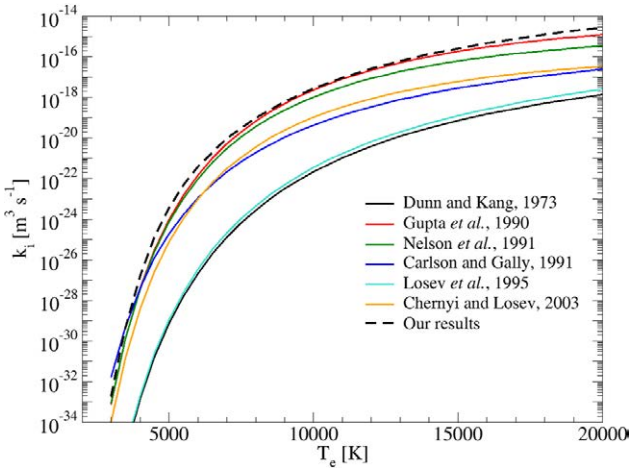

Figure 4. Comparison between the nitrogen global ionization rate coefficient k_i obtained following the procedure of section 2.3 (**- - - -**) and existing data.

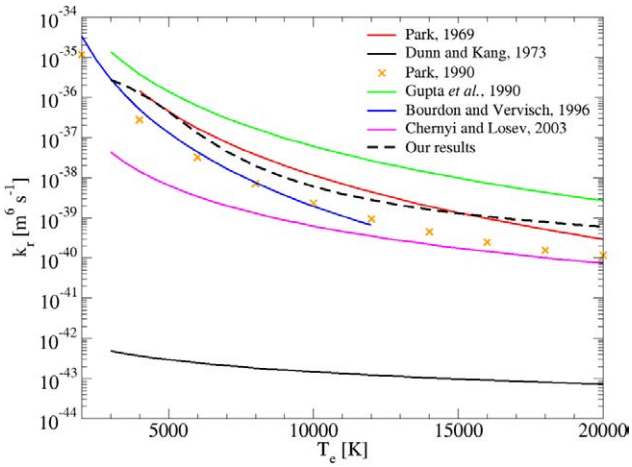

Figure 5. Comparison between the N^+ global recombination rate coefficients k_r obtained in this study (**- - - -**) and existing data.

is constant during the QSS and corresponds to the recombination global rate coefficient defined as rate coefficient k_r in

$$\frac{1}{V}\frac{\mathrm{d}N_{\mathrm{N}^+}}{\mathrm{d}t} = \frac{1}{V}\frac{\mathrm{d}N_{\mathrm{e}}}{\mathrm{d}t} = -\frac{1}{V}\frac{\mathrm{d}N_{\mathrm{N}}}{\mathrm{d}t} = -k_r\,[\mathrm{N}^+]\,\mathrm{n_e^2}. \qquad (21)$$

For T_e ranging from 3000 K to 20 000 K, the k_r values have been determined following the previous procedure. The resulting evolution of k_r with T_e is displayed in figure 5. Our results show a good agreement with most literature reference data [18, 19, 23–27]. In addition, the agreement is excellent with the experimental results of Park [26, 27]. This excellent agreement validates the theoretical approach developed in this study.

Similar calculations for ionization and recombination have been performed for carbon, oxygen and argon atoms, the results of which are displayed and discussed in [16].

2.4. Limit of the global rate coefficient concept

The previous ionization and recombination rate coefficients can be used in entry plasma CFD calculations based on Navier–Stokes codes if (1) information on species is only required, (2) the electron temperature is low, and (3) the chemical nonequilibrium is moderate. In fact, if the flow is in strong chemical nonequilibrium, the coupling between excited states emphasized previously and put forward to explain the QSS no longer takes place. Moreover, the higher the temperature T_e, the higher the excited state departure from excitation equilibrium. Therefore, the ratio k_i/k_r departs from K^S and equation (19) is not observed. We have verified this basic property and shown that k_i/k_r exceeds K^S by a factor higher than 8% for $T_\mathrm{e} > 20\,000$ K [16]. The excited states play such an important role that their behaviour has to be directly modelled. In addition, radiation may also play a significant role for high T_e values and cannot be disregarded any longer in the balance equation (5). In order to illustrate these types of conditions, the next section illustrates the elaboration of a CR model appropriate to a strong nonequilibrium situation resulting from the shock crossing in pure N_2.

3. Case 1D: shock crossing in pure N_2

3.1. Coupling of balance equations

N_2 is the main component of the Earth's atmosphere. Thus, many experimental and theoretical works have been devoted to this molecule. As a result, N_2 molecules quickly became a benchmark for atmospheric entry studies. In a Lagrangian approach, the plasma formation near the wall can be understood as the result of the shock crossing behind which the flow undergoes a strong compression. From the point of view of ground test facilities, using shock tubes therefore became one of the most relevant ways to study entry plasmas [29]. In this section, we study the case of a steady shock propagating inside a shock tube which corresponds to the shock front crossing in front of the wall by a simple change in the coordinate system.

Under typical conditions, the plasma is found in thermal and chemical nonequilibrium over a distance of several centimetres which corresponds to the order of magnitude of the SL thickness [30]. The convective time scale τ_c is consequently shorter than the characteristic time scale of the source term $[\dot{X}_i]_\mathrm{C} + [\dot{X}_i]_\mathrm{R}$ in equation (5). Therefore, each excited state i presents a behaviour less coupled than in the case of section 2 and requires an individual treatment.

The diffusion characteristic time scale is largely longer than the other ones in the balance equation (5) so that every diffusion process can be neglected. Defining the X_i mass fraction by

$$y_{X_i} = \frac{\rho_{X_i}}{\rho}, \qquad (22)$$

the X_i balance equation can be written as

$$\frac{\mathrm{d}y_{X_i}}{\mathrm{d}x} = \frac{m_{X_i}\left([\dot{X}_i]_\mathrm{C} + [\dot{X}_i]_\mathrm{R}\right)}{\rho u}. \qquad (23)$$

The flow is along the x-axis with velocity u. This equation is coupled with the momentum balance equation

$$\frac{\mathrm{d}}{\mathrm{d}x}\left(p + \rho\,u^2\right) = 0, \qquad (24)$$

Table 3. Species and states considered in the CR model presented in section 3 for pure N_2 shock crossing.

Species	States
N_2	$X\,^1\Sigma_g^+(v=0\rightarrow v_{max}=67)$, $A\,^3\Sigma_u^+$, $B\,^3\Pi_g$, $W\,^3\Delta_u$, $B'\,^3\Sigma_u^-$, $a'\,^1\Sigma_u^-$, $a\,^1\Pi_g$, $w\,^1\Delta_u$, $G\,^3\Delta_g$, $C\,^3\Pi_u$, $E\,^3\Sigma_g^+$
N_2^+	$X\,^2\Sigma_g^+$, $A\,^2\Pi_u$, $B\,^2\Sigma_u^+$, $a\,^4\Sigma_u^+$, $D\,^2\Pi_g$, $c\,^2\Sigma_u^+$
N	$^4S^o_{3/2}$, $^2D^o = (^2D^o_{5/2} +^2 D^o_{3/2})$, $^2P^o = (^2P^o_{1/2} +^2 P^o_{3/2})$, $^4P_{1/2}$,... (63 states)
N^+	$^3P_0$, $^3P_1$, $^3P_2$, $^1D_2$, $^1S_0$, $^5S^o_2$, $^3D^o_3$, $^3D^o_2$, $^3D^o_1$
e^-	—

where p is the pressure. The plasma remains weakly dense and can be considered as kinetic. As a result, pressure p can be calculated by

$$p = p_A + p_e \tag{25}$$

with $p_A = \rho k_B T_A \sum_{i\neq e^-} \frac{y_{X_i}}{m_{X_i}}$ and $p_e = \rho k_B T_e \frac{y_e}{m_e}$ owing to the thermal nonequilibrium. T_A is the kinetic temperature of heavy particles and T_e is the electron temperature.

The previous equations are finally coupled with the energy balances

$$\frac{d}{dx}\left(\frac{e_A}{\rho} + \frac{p_A}{\rho} + \frac{\rho_A}{\rho}\frac{u^2}{2}\right) = \frac{Q_{A_e} - Q_R}{\rho u} \tag{26}$$

for heavy particles and

$$\frac{d}{dx}\left(\frac{e_e}{\rho} + \frac{p_e}{\rho} + \frac{\rho_e}{\rho}\frac{u^2}{2}\right) = -\frac{Q_{A_e}}{\rho u} \tag{27}$$

for electrons. In equations (26) and (27), $\rho_A = \rho \sum_{i\neq e^-} y_{X_i}$ and $\rho_e = \rho y_e$. e_A/ρ and e_e/ρ are the specific internal energy for heavy particles and electrons, respectively. Finally, Q_{A_e} is the energy exchanged per unit volume inside the flow between heavy particles and electrons (due to the elastic and inelastic/superelastic collisions) and Q_R is the energy lost by the flow per unit volume through radiation.

3.2. CR source term

Upstream from the shock front (subscript 1), the incident cold gas contains N_2 molecules only. The upstream Mach number $\mathcal{M}_1 = u_1/c_1$, where c_1 is the upstream speed of sound, can easily reach $\mathcal{M}_1 = 30$. Under these conditions, the flow can be strongly dissociated and ionized. The dissociation results from stepwise vibrational excitation. Vibrational states of N_2 have therefore to be individually accounted for. Moreover, electronic excited states can be populated and lead to significant radiative losses through deexcitation. As a result, the model is electronic and vibrational specific. The energy diagram also takes into account atoms, molecules and (atomic and molecular) ions which can be formed until equilibrium (or steady conditions in the case of strong radiative losses) is reached. Note that a degeneracy weighted procedure has been used to lump together real levels in fictitious levels to obtain the final number of N and N^+ levels considered in the model [31]. These species and their states are listed in table 3. It is worth noting that the number of states considered in the present section is less than that used in section 2.3. This reduction does not change the dynamics shown in the following since $\Delta E_l \ll k_B T_A$.

The shock front is considered as a discontinuity across which the flow is frozen under the upstream chemical conditions. At this discontinuity in $x = 0$, Mach number, pressure, kinetic temperature of heavy particles and velocity suddenly jump from ($\mathcal{M}_1$, p_1, T_{A1}, u_1) to ($\mathcal{M}_2$, p_2, T_{A2}, u_2), respectively. This gap respects the classical Rankine–Hugoniot equations [32]. These equations assume an infinitely short characteristic time scale to reach the Maxwellian distribution for translation of any type of particle. They are based on the mass, momentum and energy balances across the discontinuity. They lead to values of T_{A2} ranging typically from 10 000 to 70 000 K. Electron temperature is frozen across the shock front because the electron gas sound speed exceeds largely the incident gas velocity which means that the flow is electronically subsonic [33].

The collisional elementary processes taken into account in the source term of equations (23), (26) and (27) are due to electron impact leading to excitation/deexcitation (9) and to ionization/recombination (10) of atoms or molecules. Since T_A is high and the ionization degree negligibly small at $x = 0$, inelastic collisions with heavy particles are also taken into account. In particular, they are responsible for the stepwise vibrational excitation through vibration–translation processes with atoms (VTa) and molecules (VTm) leading to the dissociation (VTa-d and VTm-d processes). Vibration–vibration (VV) elementary processes between molecules are also taken into account. Charge exchange processes can play a significant role and are accounted for. Particular processes between electrons and heavy particles are also accounted for, such as dissociative recombination, vibration-electron (Ve) processes and elastic collisions resulting from the thermal nonequilibrium. Only the vibrational excitation/deexcitation processes under N and electron-induced collisions account for multi-quanta jumps since the contribution of other collision partners is negligibly small [35]. The rate coefficient set of Armenise *et al* [35] and Esposito *et al* [36] based on a quasi-classical trajectory approach for the vibrational processes due to heavy particle impact has been implemented. No study on the sensitivity of the results to the database has been performed in this work. The *Phys4Entry* European project will shortly provide new data which will be tested in future works. Table 4 summarizes the different inelastic processes and the related sources from which the different rate coefficients have been derived. The backward rate coefficients are derived from the forward rate coefficients using the detailed balance principle.

The following radiative systems are taken into account in the source term: (1) the first and second positive systems of N_2 (transitions $B\,^3\Pi_g \rightarrow A\,^3\Sigma_u^+$ and $C\,^3\Pi_u \rightarrow B\,^3\Pi_g$,

Table 4. Elementary processes considered in the CR model presented in section 3 for pure N_2 shock crossing. i, j and k symbolize electronic excited states.

Type	Elementary processes	References
Vibrational processes	$N_2(X, v) + e^- \rightarrow N_2(X, w) + e^-$	[34]
	$N_2(X, v) + e^- \rightarrow 2\,N(^4S^o_{3/2}) + e^-$	[34]
	$N_2(X, v) + (N_2 \text{ or } N) \rightarrow N_2(X, w) + (N_2 \text{ or } N)$	[35, 36]
	$N_2(X, v) + N(^4S^o_{3/2}) \rightarrow 3\,N(^4S^o_{3/2})$	[35, 36]
	$N_2(X, v_{max}) + N_2 \rightarrow 2\,N(^4S^o_{3/2}) + N_2$	[35, 36]
	$N_2(X, v_1) + N_2(X, v_2) \rightarrow N_2(X, w_1) + N_2(X, w_2)$	[35]
Electronic excitation	$N_2(i) + e^- \rightarrow N_2(j) + e^-$	[37]
	$N_2(i) + (N_2 \text{ or } N) \rightarrow N_2(j) + (N_2 \text{ or } N)$	[37–39]
	$N_2^+(i) + e^- \rightarrow N_2^+(j) + e^-$	[40]
	$N(i) + e^- \rightarrow N(j) + e^-$	[14, 41]
	$N(i) + (N_2 \text{ or } N) \rightarrow N(j) + (N_2 \text{ or } N)$	[37–39, 42]
	$N^+(i) + e^- \rightarrow N^+(j) + e^-$	[14]
	$N^+(i) + (N_2 \text{ or } N) \rightarrow N^+(j) + (N_2 \text{ or } N)$	[37–39]
Excitation transfer	$N_2(A) + N_2(A) \rightarrow N_2(X) + N_2(B)$	[37]
	$N_2(A) + N_2(A) \rightarrow N_2(X) + N_2(C)$	[43]
	$N_2(A) + N_2(B) \rightarrow N_2(X) + N_2(C)$	[42]
	$N_2(A) + N(^4S^o_{3/2}) \rightarrow N_2(X) + N(^2P^o)$	[37]
	$N_2(B) + N(^4S^o_{3/2}) \rightarrow N_2(X) + N(^2P^o)$	[42]
	$N_2(C) + N(^4S^o_{3/2}) \rightarrow N_2(X) + N(^2P^o)$	[42]
Dissociation	$N_2(i \neq X) + e^- \rightarrow N(j) + N(k) + e^-$	[40]
	$N_2^+(i) + e^- \rightarrow N(j) + N^+(k) + e^-$	[40]
Ionisation	$N_2(i) + e^- \rightarrow N_2^+(j) + 2\,e^-$	[40]
	$N_2(i) + (N_2 \text{ or } N) \rightarrow N_2^+(j) + e^- + (N_2 \text{ or } N)$	[38, 39]
	$N(i) + e^- \rightarrow N^+(j) + 2\,e^-$	[14, 41, 44]
	$N(i) + (N_2 \text{ or } N) \rightarrow N^+(j) + e^- + (N_2 \text{ or } N)$	[38, 39]
Charge exchange	$N_2(X) + N^+(^3P_0) \rightarrow N_2^+(X) + N(^4S^o_{3/2} \text{ or } ^2P^o)$	[43]
	$N_2(X) + N^+(^3P_0) \rightarrow N_2^+(A) + N(^4S^o_{3/2})$	[43]
Dissociative recombination	$N_2^+(X) + e^- \rightarrow N(^4S^o_{3/2}) + N(^2D^o \text{ or } ^2P^o)$	[45]
	$N_2^+(X) + e^- \rightarrow N(^2D^o) + N(^2D^o)$	[45]
Radiation	$N_2(B\,^3\Pi_g) \rightarrow N_2(A\,^3\Sigma_u^+) + h\nu$ (first positive)	[41, 46]
	$N_2(C\,^3\Pi_u) \rightarrow N_2(B\,^3\Pi_g) + h\nu$ (second positive)	[41, 46]
	$N_2^+(B\,^2\Sigma_u^+) \rightarrow N_2^+(X\,^2\Sigma_g^+) + h\nu$ (first negative)	[41, 46]
	$N(i) \rightarrow N(j < i) + h\nu$	[15]
	$N^+(i) \rightarrow N^+(j < i) + h\nu$	[15]

respectively) and (2) the first negative system of N_2^+ (transition $B\,^2\Sigma_u^+ \rightarrow X\,^2\Sigma_g^+$). N and N^+ lines are also implemented, the equivalent Einstein coefficients of which have been calculated from the NIST database. The degeneracy weighted procedure is used to calculate these equivalent Einstein coefficients since real levels are lumped together in fictitious levels. In addition, escape factors are used because transitions are not necessarily optically thin [47].

3.3. Post-shock relaxation

The conditions retained to illustrate the results obtained from the previous CR model correspond to those of the FIRE (Flight Investigation of Reentry Environment) II probe flight. This probe was equipped with spectral and total radiometers, and calorimeters able to measure the TPS heat flux on both front and rear sides of the probe [48]. Launched in 1965 in the framework of the Apollo program, this probe experienced a reentry at hypersonic velocity with $\mathcal{M}_1 > 30$. Although the experiment was performed 50 years ago, the FIRE II test case is still intensively studied. This test case has led to many theoretical and experimental studies, especially in pure N_2 since this molecule is the main component of the Earth's atmosphere. Shock tube experiments in particular have been performed [49].

The calculated shock tube-like flow corresponds to the FIRE II stagnation streamline. From the typical conditions $\mathcal{M}_1 = 33$, $p_1 = 33$ Pa, $T_{A1} = 255$ K corresponding to time $t = 1640$–1641 s from the launch of the probe during the reentry at an altitude of $z = 59$ km [51], heavy particle kinetic temperature behind the shock front reaches 50 000 K while the chemical composition and the electron temperature are the same as in the upstream flow. These conditions have been chosen because they have been widely studied theoretically [29] and experimentally [50] since they are close to the peak heating undergone by the TPS of the probe. The flow is thus

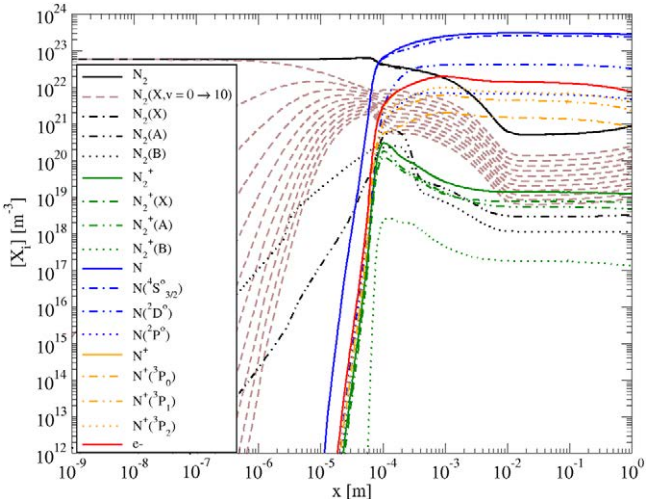

Figure 6. Relaxation of chemical composition behind a shock front in N_2 with the upstream conditions $\mathcal{M}_1 = 33$, $p_1 = 33$ Pa, $T_{A1} = 255$ K related to the trajectory point $t = 1\,640$–$1\,641$ s of the FIRE II flight experiment [51].

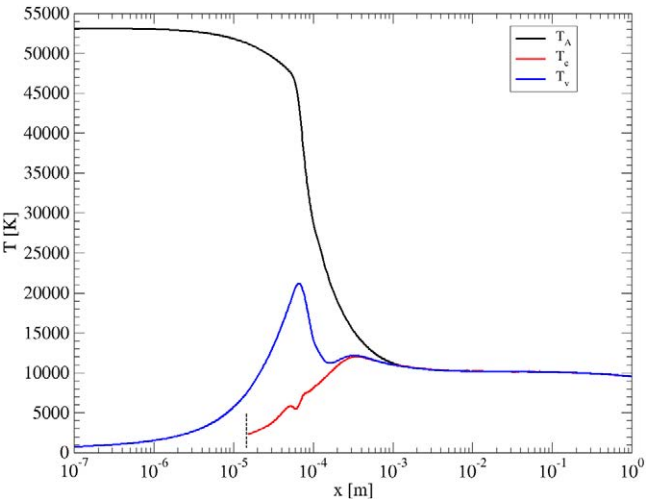

Figure 7. Spatial evolution of characteristic temperatures of the flow behind the shock front under the conditions of figure 6. For $x \lesssim 10^{-5}$ m, the electron density is negligibly small: electron temperature T_e is irrelevant. Beyond the vertical black dashed segment, n_e is high enough ($n_e > 10^8$ m^{-3}) and T_e is plotted.

in chemical and thermal nonequilibrium. Then, elementary processes listed in table 4 are no longer counterbalanced by the corresponding backward elementary processes and lead to the relaxation displayed in figure 6. The underlying dynamics cannot be explained without analysing the temperature time evolution of the flow illustrated by figure 7.

The high temperature of N_2 molecules just behind the shock front leads to the progressive excitation of their vibrational levels. This excitation is illustrated by the increase in the vibrational temperature arbitrarily defined in our case as the excitation temperature of the first five vibrational levels

$$T_v = -\frac{1}{k_B \left[\frac{d}{dE_{X,v}} (\ln[N_2(X, v)])\right]_{lsl}} \qquad (28)$$

where lsl means that the derivative is the slope of the least square line and $E_{X,v}$ is the vibrational energy. The vibrational temperature is thus defined like any excitation temperature using a Boltzmann plot. Since the low-lying levels are the most populated vibrational levels, this excitation temperature is representative of the energy stored in the vibrational motion and can be directly compared with experimental results when they are available.

The vibrational excitation requires energy taken from translation and explains the slight decrease in T_A. The set of vibrational elementary processes listed in table 4 allows the dissociation of N_2 in N atoms, the density of which undergoes a strong increase near $x = 10^{-5}$ m. Since this global dissociation is strongly driven by the vibrational elementary processes, the dissociation degree does not reach significant values before the vibrational temperature has sufficiently increased. In the meantime, the heavy particle-induced collisions lead to the ionization of the flow. Electronic excitation also takes place. The electron temperature concept is irrelevant for $x \lesssim 10^{-5}$ m since electron density is negligibly small ($n_e < 10^8$ m^{-3}) [42]. Nevertheless, T_e increases afterwards owing to the vibration-electron and inelastic processes. When the mole fraction of electrons reaches a value around 10^{-5} at $x \simeq 5 \times 10^{-5}$ m, electron-induced processes take over. Afterwards, the coupling of the vibrational levels is complete and they behave as a whole. The vibrational thermal coupling is achieved at $x \simeq 4 \times 10^{-4}$ m with T_e, and at $x \simeq 10^{-3}$ m with T_A. The final step is then characterized by the end of the dissociation phase until $x \simeq 10^{-2}$ m beyond which a quasi-uniform zone is observed. This zone corresponds to local thermodynamic equilibrium because the flow radiative losses are negligibly small. Nevertheless, these losses play a role because they induce a very slow relaxation until the plasma is uniform. Note that a geometrical characteristic length of 5 cm has been chosen to calculate escape factors. This length corresponds to the typical radius of shock tubes and to the usual thickness of the SL previously described in section 1.

It is interesting to further study how the plasma reaches equilibrium. The Boltzmann diagram for N atoms is plotted in figure 8 for $x = 3 \times 10^{-5}$, 7×10^{-5}, 10^{-4}, 5×10^{-4} and 10^{-3} m. We can see the progressive coupling of the population densities starting from a significant underpopulation with respect to equilibrium calculated at the translation temperature of the main collision partner. Such an underpopulation during ionization has already been discussed in section 2.3 about the calculation of nitrogen ionization global rate coefficients. In the present case of post-shock flow calculation, the common treatment of the energy and momentum balances with the mass balance does not affect this fundamental characteristic. But the situation is complicated by collisions with heavy particles, whose temperature remains high. We have also plotted in figure 8 dashed lines corresponding to partial equilibrium with an excitation temperature (calculated in the same way as equation (28)) of $T_{exc} = 8000$, 11 000 and 28 000 K. These values correspond to the translation temperature of the main inelastic collision partner for the x-position concerned. We see that, starting from a significant dispersion around a distribution with $T_{exc} \simeq T_A$, the excited states close to the ionization limit reach excitation equilibrium when the thermal equilibrium

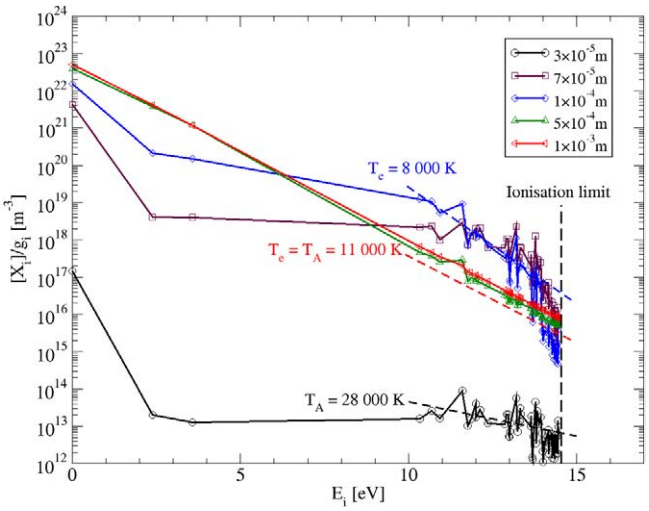

Figure 8. Boltzmann plot of N atoms at $x = 3 \times 10^{-5}$, 7×10^{-5}, 10^{-4}, 5×10^{-4} and 10^{-3} m under the conditions of figure 6. In dashed lines are plotted distributions corresponding to equilibrium at the translation temperature of heavy particles or electrons of the x-position concerned. The red dashed line is plotted under the actual distribution at $x = 10^{-3}$ m for clarity.

($T_e = T_A$) is achieved. Although many transitions are optically thin, the departure from the Boltzmann equilibrium is negligibly small for $x = 10^{-3}$ m. Collisions strongly constrain the plasma to equilibrium.

The case of post-shock flows in N_2–O_2 mixtures related to entry into the Earth's atmosphere has been treated recently by Panesi *et al* [52, 53] using the concept of global dissociation or recombination. The attention was focused on the behaviour of excited electronic levels of atoms and molecules. These works constitute an important step in the understanding of plasmas produced by shockwaves. Another more complete model accounting for the vibrational states of N_2, O_2, NO (obtained by Zeldovich neutral exchange processes) and electronic excited states of Ar has been elaborated [54]. For the moment, only relaxation calculations at constant pressure and temperature can be performed. Its coupling with energy and momentum balances for post-shock calculations is in progress.

4. Pseudo-2D case: CO_2 flows in HEWTs

4.1. Treatment of the balance equation

In contrast to the case of Earth atmospheric reentries for which many experiments have been performed, the case of Martian atmospheric entries has been much less studied. Owing to the distance between Earth and Mars, it is impossible to send specific probes such as FIRE II to study the entry by itself. It is more convenient to equip the landing spacecraft with sensors as often as possible and to therefore profit from any Martian entry to collect information. The successful entry experienced by the Curiosity rover on 5 August 2012 illustrates this philosophy since its TPS was equipped with 14 temperature and pressure instruments in order to improve understanding of the entry environment and material response [55].

Nevertheless, a complete study has to be performed prior to the actual landing. In this context, experiments performed in ground test facilities are a valuable alternative. In addition to experiments in shock tubes mentioned in section 3, those performed in HEWTs using high frequency power supplies are particularly valuable. These HEWTs generate a subsonic and axisymmetric plasma jet across a hole in a test chamber maintained at a sufficiently low pressure level using a high rate pumping system. A plasma similar to the one obtained near the edge of boundary layers close to the TPS can be formed under steady, therefore comfortable, conditions. TPS materials can then be tested and boundary layers can be probed. This type of experiment cannot be performed with shock tubes owing to their short running time scale (several tenths of microseconds [56]).

The composition of the plasma interacting with a material used for TPS has to be determined, especially for CO_2. In fact, this triatomic molecule leads to many other species such as CO, C_2, O_2, C and O when the dissociation degree becomes significant [57]. The relative density of these species plays a significant role in the parietal heat flux. In addition, the radiative losses are higher than those observed in air under similar conditions. The flow can then significantly depart from equilibrium. A detailed study of the flow is therefore required.

In parallel with experiments performed in the VKI [58] and CORIA [59] HEWTs, we have elaborated a time-dependent CR model devoted to this detailed study. In addition, this model provides an estimate of the CO_2 flow characteristic time scale to reach steady state. The mass balance is not treated under the form of equation (1) owing to the complexity of the source term. This balance equation is therefore modified as follows.

Equation (1) is averaged over the cross section Σ of the flow, the radius R of which evolves slightly with the longitudinal coordinate x. This property $\mathrm{d}\Sigma/\mathrm{d}x \simeq 0$ results from the weak opening of the flow. The resulting cylindrical symmetry leads to approximate any averaged value $\bar{\rho}_{X_i}(x,t)$ over Σ by

$$\bar{\rho}_{X_i}(x,t) = \rho_{X_i}(x,r,t)\frac{B}{J_0\left(\lambda_1 \frac{r}{R}\right)}, \tag{29}$$

where $\lambda_1 = 2.405$ is the first root of the zeroth-order Bessel function J_0 and $B = \frac{2}{R^2}\int_0^R J_0(\lambda_1 \frac{r}{R})\, r\, \mathrm{d}r$ [60].

The density gradients inside the jet are weak. In addition, the excited state number density is weak with respect to that of the corresponding species ground state. The diffusion phenomena normally modelled by the Stefan–Maxwell laws [61] can be simplified by considering the classical Fick's law involving the species-dependent D_{X_i} diffusion coefficient, which leads to

$$\frac{1}{J_0}\frac{\partial}{\partial r}\left(\bar{J}_{X_i} J_0\right) = \lambda_1^2 D_{X_i}\frac{\bar{\rho}_{X_i}}{R^2}. \tag{30}$$

The previous simplification does not basically change the estimate of the diffusion characteristic time scale [62]. Neglecting the longitudinal diffusion, the balance equation becomes

$$\frac{\partial \bar{\rho}_{X_i}}{\partial t} + \frac{\partial}{\partial x}\left(\bar{\rho}_{X_i} u\right) + \lambda_1^2 D_{X_i}\frac{\bar{\rho}_{X_i}}{R^2} = \bar{\dot{\rho}}_{X_i}. \tag{31}$$

Table 5. Species and states considered in the CR model presented in section 4 for pure CO_2 HEWT plasmas. Electrons are considered as collision partners only for inelastic processes.

Species	States
CO_2	$X\,^1\Sigma_g^+$
CO	$X\,^1\Sigma^+$, $a\,^3\Pi$, $a'\,^3\Sigma^+$, $d\,^3\Delta_i$, $e\,^3\Sigma^-$, $A\,^1\Pi$, $D\,^1\Delta^-$, $b\,^3\Sigma^+$, $B\,^1\Sigma^+$
C_2	$X\,^1\Sigma_g^+$, $a\,^3\Pi_u$, $b\,^3\Sigma_g^-$, $A\,^1\Pi_u$, $c\,^3\Sigma_u^+$, $d\,^3\Pi_g$, $C\,^1\Pi_g$, $e\,^3\Pi_g$, $D\,^1\Sigma_u^+$
O_2	$X\,^3\Sigma_g^-$, $a\,^1\Delta_g$, $b\,^1\Sigma_g^+$, $A\,^3\Sigma_u^+$, $b\,^3\Sigma_u^-$
C	$^3P_0$, $^3P_1$, $^3P_2$, $^1D_2$, $^1S_0$, $^5S_2^o$, $^3D_0^o$, $^3D_1^o$, $^3D_2^o$,... (268 states)
O	$^3P_2$, $^3P_1$, $^3P_0$, $^1D_2$, $^1S_0$, $^5S_2^o$, $^3S_1^o$, $^5P_1$, $^5P_2$,... (127 states)
e^-	—

The excited state number density gradients along the x-axis being negligibly small, we have

$$\frac{\partial}{\partial x}\left(\bar{\rho}_{X_i}\,u\right) \simeq \bar{\rho}_{X_i}\frac{\partial u}{\partial x} \tag{32}$$

where the term $\partial u/\partial x$ can be reasonably approximated by $-u/x$ since the flow is weakly compressible, laminar and quasi-isothermal [63]. At the distance from the hole of injection equal to R in order of magnitude, the final form of the balance equation for the number densities is

$$\left(\frac{\partial[\bar{X}_i]}{\partial t}\right)_{x\sim R} \simeq \left(\frac{[\bar{X}_i]\,u}{R} - \lambda_1^2 D_{X_i}\frac{[\bar{X}_i]}{R^2} + [\dot{\bar{X}}_i]_C + [\dot{\bar{X}}_i]_R\right)_{x\sim R}. \tag{33}$$

The right-hand side of the previous equation depends on time since densities are considered at a given location. This equation can then be written under the form of the differential equation

$$\left(\frac{\mathrm{d}[\bar{X}_i]}{\mathrm{d}t}\right)_{x\sim R} \simeq \left(\frac{[\bar{X}_i]\,u}{R} - \lambda_1^2 D_{X_i}\frac{[\bar{X}_i]}{R^2} + [\dot{\bar{X}}_i]_C + [\dot{\bar{X}}_i]_R\right)_{x\sim R}. \tag{34}$$

The resulting set of time-dependent equations can be solved and leads to an estimation of the characteristic time scale required by the mixture to reach a steady state.

4.2. Elementary processes

In pure CO_2 plasmas produced in HEWTs, the radiative signature is mainly due to CO and C_2 bands, and to C and O lines [64]. The CR model development reported in this section is therefore focused on the excited states of these species. Table 5 lists the molecular states considered. The dissociation of CO_2 is considered as taking place inside the inductively coupled zone. As in the case of N_2 used as working gas, its dissociation degree is assumed close to its equilibrium value a few centimetres downstream before entering the test chamber [65]. Therefore, the development of a vibrational specific model of CO_2 is not required and a global dissociation rate coefficient can be used. We assumed that all vibrational modes are coupled together with the same vibrational temperature T_v equal to electron temperature T_e. The vibrational temperature of the diatomic molecules is also assumed equal to T_e. Electrons are considered as collision partners only for inelastic processes. The ion effect is totally ignored.

Table 6 presents the different collisional and radiative elementary processes taken into account in our model. In contrast to the case of collisional processes involving CO for which many rate coefficients are available, those involving C_2 have been less studied. We have stated hypotheses for most of them.

The case of collisions corresponding to optically allowed (OAT) or forbidden (OFT) transitions is treated separately and the concept of efficiency is used to estimate the collision partner-dependent rate coefficient. Deexcitation processes due to particle M induced collisions are assumed driven by the rate coefficient

$$k^M(T) = \eta_M\sqrt{\frac{8k_B T}{\pi\mu}}\sigma_{10^4\,\mathrm{K}}\left(\frac{T}{10^4}\right)^m \tag{35}$$

where η_M is the efficiency of M as collision partner (with the Maxwellian distribution at T), μ is the reduced mass between collision partners, $\sigma_{10^4\,\mathrm{K}}$ is the mean cross section at 10^4 K and m an exponent. If the deexcitation process corresponds to an OAT, the rate coefficient is high and the value $m = 0.5$ is stated. Conversely, if the deexcitation process corresponds to an OFT, the rate coefficient is lower and the value $m = 0$ is adopted. The cross section $\sigma_{10^4\,\mathrm{K}}$ is put equal to 4×10^{-19} m^2 for allowed transitions and $\sigma_{10^4\,\mathrm{K}} = 10^{-20}$ m^2 for forbidden transitions. These assumptions are compatible with mean behaviours put forward by Surzhikov [66], Park [67] and Losev and Shatalov [77]. Park also showed that atoms are 20 times as efficient as molecules in the excitation of N_2 and O_2. We therefore assumed $\eta_{CO_2} = \eta_{CO} = \eta_{O_2} = \eta_{C_2} = 1 = \eta_C/20 = \eta_O/20$. For electrons, the cross sections proposed by Drawin [14] are used assuming that atoms and molecules have the same behaviour when no experimental data are available (see the review of Brunger and Buckman [78]).

For the dissociation, the rate coefficient is written in the form

$$k^M(T, T_v) = \eta_M A\left(1 - \mathrm{e}^{-\frac{\omega_e}{k_B T_v}}\right)\mathrm{e}^{-\frac{E_d}{k_B T_v}+3\left(\frac{T}{T_v}-1\right)} \tag{36}$$

by analogy with the nonequilibrium vibration–translation dissociation rate coefficient of N_2 and O_2 used by Losev and Shatalov [77]. ω_e is the first vibrational spectroscopic constant and the dissociation energy of the involved state is E_d. The efficiency of atom-induced dissociation is assumed eight times as high as for molecules ($\eta_{CO_2} = \eta_{CO} = \eta_{O_2} = \eta_{C_2} = 1 = \eta_C/8 = \eta_O/8$) and $A = 10^{-15}$ m^3 s^{-1} which allows a

Table 6. Elementary processes considered in the CR model presented in section 4 for pure CO_2 jet in HEWTs produced by HF power supplies. i, j and k symbolize electronic excited states.

Type	Elementary processes	References
Excitation/	$CO(a\,^3\Pi) + CO_2 \rightarrow CO(X\,^1\Sigma_g^+) + CO_2$	[66]
deexcitation	$CO(i) + (CO, O_2, O) \rightarrow CO(j > i) + (CO, O_2, O)$	[67]
	$CO(i) + M_{\neq CO,O_2,O} \rightarrow CO(j > i) + M_{\neq CO,O_2,O}$	[14, 67, 77]
	$C_2(X\,^1\Sigma_g^+) + M \rightarrow C_2(d\,^3\Pi_g) + M$	[68]
	$C_2(a\,^3\Pi_u) + CO_2 \rightarrow C_2(X\,^1\Sigma_g^+) + CO_2$	[69]
	$C_2(a\,^3\Pi_u) + O_2 \rightarrow C_2(X\,^1\Sigma_g^+) + O_2$	[70, 71]
	$C_2(a\,^3\Pi_u) + O \rightarrow C_2(X\,^1\Sigma_g^+) + O$	[72]
	$C_2(A\,^1\Pi_u) + CO_2 \rightarrow C_2(X\,^1\Sigma_g^+) + CO_2$	[73]
	$C_2(i) + M_{\neq CO_2,O_2,O} \rightarrow C_2(j > i) + M_{\neq CO_2,O_2,O}$	[39]
Exchange	$CO(a\,^3\Pi) + O \rightarrow C + O_2$	[74]
	$CO(a\,^3\Pi) + CO \rightarrow CO_2 + C$	[75]
	$C_2(d\,^3\Pi_g) + O \rightarrow CO(X\,^1\Sigma_g^+) + C$	[76]
Dissociation	$CO(i) + (CO, O_2, O) \rightarrow C(j) + O(k) + (CO, O_2, O)$	[67]
	$CO(i) + M_{\neq CO,O_2,O} \rightarrow C(j) + O(k) + M_{\neq CO,O_2,O}$	[77]
	$C_2(i) + M \rightarrow C(j) + C(k) + M_{\neq CO,O_2,O}$	[77]
Radiation	$CO(a'\,^3\Sigma^+) \rightarrow CO(a\,^3\Pi) + h\nu$ (Asundi)	[85]
	$CO(d\,^3\Delta_i) \rightarrow CO(a\,^3\Pi) + h\nu$ (triplet)	[85]
	$CO(A\,^1\Pi) \rightarrow CO(X\,^1\Sigma^+) + h\nu$ (fourth positive)	[83]
	$CO(b\,^3\Sigma^+) \rightarrow CO(a\,^3\Pi) + h\nu$ (third positive)	[83]
	$CO(B\,^1\Sigma^+) \rightarrow CO(X\,^1\Sigma^+) + h\nu$ (Hopfield–Birge)	[83]
	$CO(B\,^1\Sigma^+) \rightarrow CO(A\,^1\Pi) + h\nu$ (Angström)	[83]
	$C_2(A\,^1\Pi_u) \rightarrow C_2(X\,^1\Sigma_g^+) + h\nu$ (Philips)	[84]
	$C_2(D\,^1\Sigma_u^+) \rightarrow C_2(X\,^1\Sigma_g^+) + h\nu$ (Mulliken)	[83]
	$C_2(C\,^1\Pi_g) \rightarrow C_2(A\,^1\Pi_u) + h\nu$ (Deslandres–d'Azambuja)	[83]
	$C_2(b\,^3\Sigma_g^-) \rightarrow C_2(a\,^3\Pi_u) + h\nu$ (Ballik and Ramsay)	[83]
	$C_2(d\,^3\Pi_g) \rightarrow C_2(a\,^3\Pi_u) + h\nu$ (Swan)	[83]
	$C_2(e\,^3\Pi_g) \rightarrow C_2(a\,^3\Pi_u) + h\nu$ (Fox–Herzberg)	[83]
	$C(i) \rightarrow C(j < i) + h\nu$	[15]
	$O(i) \rightarrow O(j < i) + h\nu$	[15]

dissociation rate coefficient of $C_2(X^1\Sigma_g^+)$ close to the value of Beck and Mackie [79] when $T_v \simeq T_A$. For dissociation under impact of electron with energy ϵ, the collision cross section is assumed to behave like

$$\sigma(\epsilon) = \pi r_e^2 \left(\frac{\epsilon}{\epsilon_0}\right)^{-1}, \tag{37}$$

where ϵ_0 is the dissociation energy and r_e is the equilibrium distance of the excited state potential curve.

As far as we know, the diffusion coefficient of excited molecules listed in table 5 has not been experimentally determined. We have therefore used the well-known approach of Hirschfelder *et al* [80] to estimate this parameter. Assuming an interaction potential between collision partners of the Lennard-Jones type (rigid sphere collision cross section $\pi\sigma^2$ and potential depth ϵ), the collision integral is calculated with the usual developments [81]. Except for CO–CO interactions the potential of which has been recently calculated [82], the Lennard-Jones parameters σ and ϵ are determined using the composition rules given by Hirschfelder *et al* based on C–C and C–O interactions for C_2 and CO molecules, respectively. The interaction between CO_2 and other species is assumed similar to the CO-other species interaction, the second oxygen atom of CO_2 being assumed sufficiently far. Table 7 lists the values used for σ and ϵ.

Table 7. Rigid spheres' collision radius σ and potential depth ϵ for the calculation of the diffusion coefficient [80, 81] of the excited species in interaction with the listed collision partners.

Collision partner	σ ($\times 10^{-10}$ m)	ϵ (eV)
CO_2	3.2	0.0186
CO	3.2	0.0186
O_2	3.2	0.0186
C_2	3.2	0.0186
C	2.1	0.3399
O	2.1	0.3084

Many radiative transitions are taken into account, the radiative lifetimes of which are due to Babou [83], Kirby and Cooper [84] and da Silva [85]. The related values are given in table 8. For atomic lines, the NIST database is used. For each radiative transition, an escape factor based on Doppler broadening is calculated to estimate the self-absorption.

4.3. Relaxation time scales and convective–diffusive-CR process contributions

Two test cases are discussed in the following. They are listed in table 9. The first case (a) corresponds to a low-pressure flow at high powers and the second case (b) to a high pressure

Table 8. Radiative lifetimes for the CO and C_2 excited states.

CO($j \rightarrow i$) transitions	System	$\tau_{j\rightarrow i}$ ($\times 10^{-9}$ s)	Ref.
$a'\,^3\Sigma^+ \rightarrow a\,^3\Pi$	Asundi	10^5	[85]
$d\,^3\Delta_i \rightarrow a\,^3\Pi$	Triplet	2 500	[85]
$A\,^1\Pi \rightarrow X\,^1\Sigma^+$	fourth positive	10	[83]
$b\,^3\Sigma^+ \rightarrow a\,^3\Pi$	third positive	54	[83]
$B\,^1\Sigma^+ \rightarrow X\,^1\Sigma^+$	Hopfield–Birge	94	[83]
$B\,^1\Sigma^+ \rightarrow A\,^1\Pi$	Angstrøm	50	[84]
$C_2(j \rightarrow i)$ transitions	System	$\tau_{j\rightarrow i}$ ($\times 10^{-9}$ s)	Ref.
$A\,^1\Pi_u \rightarrow X\,^1\Sigma_g^+$	Philips	13×10^3	[83]
$D\,^1\Sigma_u^+ \rightarrow X\,^1\Sigma_g^+$	Mulliken	13	[83]
$C\,^1\Pi_g \rightarrow A\,^1\Pi_u$	Deslandres–d'Azambuja	28	[83]
$b\,^3\Sigma_g^- \rightarrow a\,^3\Pi_u$	Ballik and Ramsay	17×10^3	[83]
$d\,^3\Pi_g \rightarrow a\,^3\Pi_u$	Swan	102	[83]
$e\,^3\Pi_g \rightarrow a\,^3\Pi_u$	Fox–Herzberg	200	[83]

Table 9. Working conditions of the HEWT discussed in section 4.3. Electron parameters are estimated to $n_e \approx 10^{20}$ m^{-3} and $T_e \approx 11\,000$ K.

Working conditions	Power P (kW)	Pressure p (Pa)	Temperature T_A (K)	Total density n_T (m^{-3})	Plasma velocity u (m s^{-1})	Plasma radius R (cm)
(a)	600	1 500	9000	1.2×10^{22}	500	8
(b)	300	20 000	6000	2.4×10^{23}	80	4

at low powers. In the following, the C and O atom excitation temperature is calculated by

$$T_{\rm exc}(X_i) = -\frac{1}{k_{\rm B}\left[\frac{\rm d}{{\rm d}E_i}\left(\ln\frac{[X_i]}{g_i}\right)\right]_{\rm lsl}} \tag{38}$$

which is similar to equation (28) defining the vibrational temperature. The excitation temperature is calculated over the range $[E_{\rm ioni}-1\,{\rm eV}, E_{\rm ioni}]$. Conversely, the molecular excitation temperature of the state i is calculated by

$$T_{\rm exc}(X_i) = \frac{E_{X_i} - E_{X_1}}{k_{\rm B}\,\ln\left(\frac{Z_{\rm r}(X_i)\,Z_{\rm v}(X_i)}{Z_{\rm r}(X_1)\,Z_{\rm v}(X_1)}\,\frac{[X_1]}{[X_i]}\right)} \tag{39}$$

where subscript 1 refers to the ground electronic state, and Z_r and Z_v to the rotational and vibrational partition functions, respectively. This excitation temperature is the temperature of the plasma at equilibrium which would lead to the same $[X_i]/[X_1]$ ratio. When the plasma is in equilibrium, this excitation temperature converges to the same value whatever the excited state.

In each case, the relaxation of excited states is calculated using equation (34) starting from an excitation temperature of 10 000 K for C and O atoms [58]. Electron parameters are put equal to $n_e \approx 10^{20}$ m^{-3} and $T_e \approx 11\,000$ K as a result of the thermal conditions in the vicinity of the inductively coupled zone where the high enthalpy flow is produced [86]. Initially, excited states of CO and C_2 molecules are set equal to small population density. These initial conditions have a strong influence on the time evolution of the population densities, but they weakly influence the time required to reach the final steady state.

Figure 9 illustrates the relaxation thus obtained under the working conditions (a) focused on the $[10^{-14}; 10^{-2}]$ s interval for easier comparison with the results obtained in the second test case. After a slow evolution from the initial conditions, the excitation temperature roughly evolves around some 10^{-7} s until its final state. Before the actual steady state obtained for times largely longer than 10^{-7} s, the population densities slowly evolve as illustrated by figure 10. The whole evolution weakly depends on the convective term or the diffusive term in equation (34). This influence can be observed only by comparing the results when the values of the diffusion coefficient or the velocity are modified. These new evolutions have not been plotted on figures 9 and 10 in order to avoid an overabundance of detail. The evolution of the escape factors results from the variations of population densities. The molecular population densities are weak since the temperature

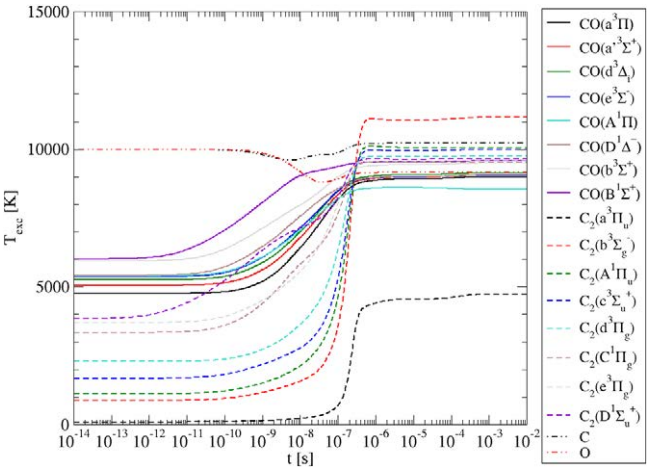

Figure 9. Time evolution of the excitation temperature of the different excited states of table 9 for the low-pressure high-power conditions (a).

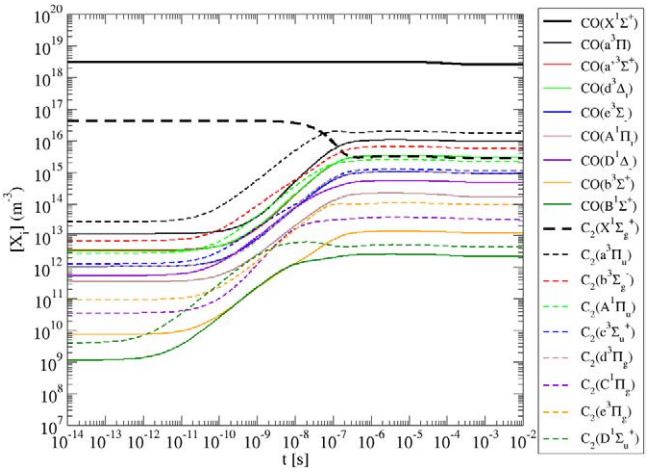

Figure 10. Evolution of the excited species number densities under the conditions of figure 9.

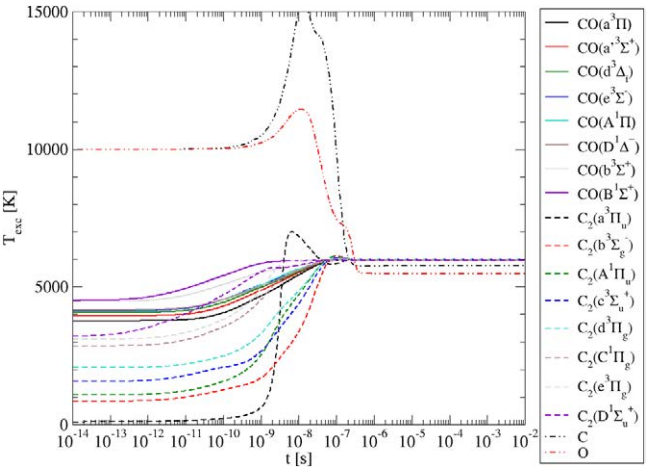

Figure 11. Time evolution of the excitation temperature of the different excited states of table 9 for the high-pressure low-power conditions (*b*).

is high and the pressure is low. Except for the fourth positive system of CO being partially self-absorbed, the plasma is optically thin for molecular systems. For atomic transitions, the O lines at 777 and 844 nm and the C line at 833 nm are self-absorbed. The other lines are all optically thin. These significant radiative losses lead to a plasma relatively far from equilibrium as illustrated by the final excitation temperatures which are different from one state to another.

The fact that population densities still evolve for times longer than $\tau = 10^{-4}$ s indicates that they are coupled over a characteristic length l_c largely higher than those required to respect the conditions of validity of equation (34). l_c can be estimated by the convective length $u\tau \approx 5$ cm at least. This corresponds to the plasma radius in order of magnitude. The conclusion is that the population number densities do not depend on local conditions only. A complete treatment of the aerodynamic field using equation (1) directly is therefore required and exceeds the scope of this paper. Finally, the present temporal approach is relevant to verify if the excited state number densities depend on the local conditions only but it cannot substitute for the solution of the energy, mass and momentum balance equations.

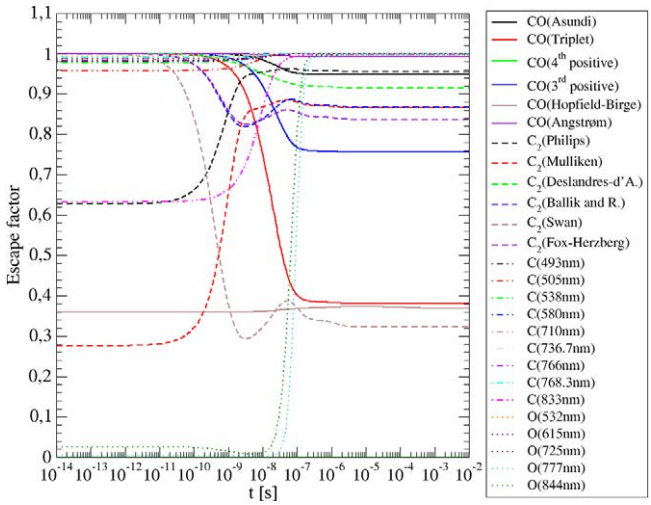

Figure 12. Same as figure 11, but for escape factors.

Figures 11 and 12 illustrate the results obtained for the test case (*b*) for the excitation temperatures and the escape factors, respectively. The characteristic time scale needed to reach the steady state is largely shorter than for the test case (*a*). At $\tau \approx 10^{-6}$ s, this steady state is reached. The convective length $l_c \approx u\tau$ is equal to approximately 100 μm. Our model can therefore be applied to the present situation. Here, we obtain a significant reduction of l_c mainly due to the increase in the collision frequency resulting from the total density n_T multiplied by a factor of 20 with respect to the test case (*a*) (see table 9). This increase in the density also leads to a higher optical thickness of the plasma as illustrated by figure 12. As in the test case (*a*), the departure from equilibrium is mainly due to radiation, and convective and diffusive transport phenomena do not play a significant role. However, in the present case, this departure is smaller since the final excitation temperature is almost equal to T_A whatever the excited state.

We extended the study to the sensitivity of the results to the adopted values for the rate coefficients. We successively increased each value by a factor of 5 and calculated the averaged excitation temperature $\overline{T_{exc}}$ and the standard deviation ΔT_{exc} for molecules in the final steady state (see table 10). This factor 5 has been chosen because it allows noticeable modifications of the results without causing changes in depth. For the test case (a), increasing the rates related to heavy particle-induced processes leads to the reduction of $\overline{T_{exc}} - T_A$ and ΔT_{exc}. Such an increase in the rate coefficients indeed constrains the mixture to be closer to equilibrium. Conversely, increasing the rate coefficients of the electron-induced processes leads in improving the coupling with electrons, which further connects T_{exc} with $T_e = 11\,000$ K and enlarge the difference $\overline{T_{exc}} - T_A$. For the test case (b), this change by the factor 5 does not basically modify the fact that the plasma is very close to equilibrium. In order to confirm the trends shown by the previous calculations, an effort in the theoretical calculation of the excitation cross sections of molecules under electron or heavy particle impact could be particularly valuable, for instance in the framework of the *Phys4Entry* project.

Table 10. Sensitivity of the results of the CR model presented in section 4 to a magnification of factor 5 of certain rate coefficients, the rate coefficients referenced in table 6 remaining unchanged. Deviation of the averaged molecular excitation temperature $\overline{T_{\rm exc}}$ from temperature T_A and standard deviation $\Delta T_{\rm exc}$. For test cases (a) and (b) without factor 5, the related values for ($\overline{T_{\rm exc}} - T_A$, $\Delta T_{\rm exc}$) are (216 K, 1 292 K) and (−5.34 K, 10.16 K), respectively.

Process	Type of transition	Collision partner	Working conditions (a) $\overline{T_{\rm exc}} - T_A$ (K)	Working conditions (a) $\Delta T_{\rm exc}$	Working conditions (b) $\overline{T_{\rm exc}} - T_A$ (K)	Working conditions (b) $\Delta T_{\rm exc}$
Excitation	OAT	Heavy particles	126	1 055	−1.73	2.85
	OFT	Heavy particles	200	904	−2.96	5.71
	OAT	Electrons	501	1724	−4.42	8.10
	OFT	Electrons	533	1086	−5.17	9.83
Dissociation	—	Heavy particles	177	1249	−5.06	10.22
Dissociation	—	Electrons	184	1324	−5.34	10.16

Comparisons between the present results and those derived from experiments in HEWTs of the Von Karman Institute and CORIA will be performed soon under rather low pressure conditions. They will contribute to validate the set of elementary data used in the present section. These data will then be used in the elaboration of a CR model for CO_2–N_2 mixtures able to be implemented in balance equations similar to equations (22)–(27) to simulate post-shock relaxations for Martian entries.

5. Conclusion

In this paper, we have given an insight into the capabilities of collisional–radiative models for the analysis of nonequilibrium plasmas. For the purpose of understanding the underlying dynamics involved in plasma flows related to planetary atmospheric entries, the elaboration of three specific collisional–radiative models has been reported.

In order to identify over a sufficiently large temperature range global rate coefficients which can be used in simplified computational fluid dynamics, a first model has been elaborated. Ionization and recombination of nitrogen atoms under electron impact have been investigated in particular. The model allows one to put forward quasi-steady states for which the global rate coefficient concept is relevant. The values thus derived are in good agreement with reference data and extend a part of them to wider temperature ranges. A departure from the Saha equilibrium constant increasing with temperature has been observed for the ratio between ionization and recombination rate coefficients. This illustrates the limit of the validity of the use of a global rate coefficient.

A second collisional–radiative model has been elaborated for simulating the plasma relaxation after the crossing of a strong shock front in a nitrogen molecule cold gas considered as a benchmark situation. The vibrational states of the ground electronic state of N_2 and the electronic excited states of N_2 and N_2^+ molecules are taken into account as well as the electronic excited states of N and N^+. A complete detailed chemistry has been reported. This vibrational and electronic specific model has been implemented in the flow equations (number densities, momentum and energy balances) coupled with radiative elementary processes. The flow relaxation takes place over several millimetres. Electronic excited states of atomic nitrogen present a complex dynamics resulting from collisions due to heavy particles and electrons. Radiation weakly influences the plasma relaxation in the situation studied.

The third collisional–radiative model reported in this paper concerns the analysis of the CO_2 plasmas produced in high enthalpy wind tunnels to test materials used for thermal protection systems. The characteristic time scale to reach a steady state strongly depends on the pressure level of the flow. The excitation nonequilibrium of the plasma is mainly due to the radiative losses while diffusive and convective contributions remain negligibly small.

All these models required numerous elementary data and their elaboration underlines the importance of their reliability.

We can give some perspectives to the work presented here. These CR models have to be generalized in order to provide information on global dissociation/recombination rate coefficients and their time scales to describe the shock layer or the boundary layer chemistry in multidimensional simulations. Complete kinetic mechanisms involving specific vibrational and electronic elementary processes have to be also identified in order to allow at least 1D flow numerical simulations on the stagnation streamline. They should be implemented outside the limiting framework of the Rankine–Hugoniot assumptions. These models should be included in shock-capturing approaches which are more realistic than the classical Rankine–Hugoniot approach. These works are in progress.

Acknowledgments

The authors wish to thank the French Spatial Agency CNES, the 'Région Haute-Normandie', the European project *Phys4Entry* (Seventh Framework Programme), the European Space Agency, and the Von Karman Institute for their financial support. They also thank Dr Yacine Babou and Mr Damien Lequang from VKI for valuable discussions and common works on the section 4.3.

References

[1] Hankey W L 1988 *Re-Entry Aerodynamics* (*AIAA Education Series*) (Washington, DC: AIAA Inc.)

[2] Anderson J D 1989 *Hypersonic and High Temperature Gas Dynamics* (New York: McGraw-Hill)
[3] Druguet M-C 2010 *Shock Waves* **20** 251
[4] Olynick D R *et al* 1995 *J. Thermophys. Heat Transfer* **9** 586
[5] Bucchignani E and Pezzella G 2010 *Math. Comput. Simul.* **81** 565
[6] Hash D, Olejniczak J, Wright M, Prabhu D, Pulsonetti M, Hollis B, Gnoffo P, Barnhardt L, Nompelis I and Candler G 2007 *45th AIAA Aerospace Sciences Meeting and Exhibit (Reno, NV)* 2007-605 p 1
[7] Rat V, Murphy A B, Aubreton J, Elchinger M F and Fauchais P 2008 *J. Phys. D: Appl. Phys.* **41** 183001
[8] Bourdon A and Bultel A 2008 *J. Thermophys. Heat Transfer* **22** 168
[9] Lamet J-M, Babou Y, Riviere P, Perrin M-Y and Soufiani A 2008 *J. Quant. Spectrosc. Radiat. Transfer* **109** 235
[10] Walpot L M, Caillault L, Molina R C, Laux C O and Blanquaert T 2006 *J. Thermophys. Heat Transfer* **20** 663
[11] Park C, Howe J T, Jaffe R L and Candler G V 1994 *J. Thermophys. Heat Transfer* **8** 9
[12] Capitelli M *et al* 2007 *Plasma Sources Sci. Technol.* **16** 830
[13] Capitelli M *et al* 2011 *Plasma Phys. Control. Fusion* **53** 124007
[14] Drawin H W 1966 *Collision and Transport Cross Sections* EUR-CEA-FC 383
[15] www.nist.gov/pml/data/asd.cfm
[16] Annaloro J, Morel V, Bultel A and Omaly P 2012 *Phys. Plasmas* **19** 073515
[17] Bultel A, van Ootegem B, Bourdon A and Vervisch P 2002 *Phys. Rev.* E **65** 046406
[18] Dunn M G and Kang S W 1973 *Theoretical and Experimental Studies of Reentry Plasmas* NASA CR 2232
[19] Gupta R N, Yos J M, Thompson R A and Lee K P 1990 *A Review of Reaction Rates and Thermodynamic and Transport Properties for an 11 Species Air Model for Chemical and Thermal Nonequilibrium Calculations to 30 000 K* NASA RP 1232
[20] Nelson H F, Park C and Whiting E E 1991 *J. Thermophys.* **5** 157
[21] Carlson L A and Gally T A 1991 *J. Thermophys.* **5** 9
[22] Losev S A, Makarov V N and Pogosbekyan M Y 1995 *Fluid Dyn.* **30** 299
[23] Chernyi G G and Losev S A 2003 *Problems of Aerothermoballistics, Radiation Gasdynamics, Heat and Mass Transfer for Planet Sample Return Missions* ISTC 1549-00
[24] Park C 1990 *Nonequilibrium Hypersonic Aerothermodynamics* (New York: Wiley)
[25] Bourdon A and Vervisch P 1996 *Phys. Rev.* E **54** 1888
[26] Park C 1968 *AIAA J.* **6** 2090
[27] Park C 1969 *AIAA J.* **7** 1653
[28] Bar-Shalom A, Klapisch M and Oreg J 2001 *J. Quant. Spectrosc. Radiat. Transfer* **71** 169
[29] Panesi M 2009 *Physical Models for Nonequilibrium Plasma Flow Simulations at High Speed Re-Entry Conditions* (Rhode-Saint-Genese: Von Karman Institute for Aerodynamics)
[30] Broc A, Joly V, Lafon J P and Marmignon C 1998 *Astrophys. Space Sci.* **260** 29
[31] Morel V, Bultel A and Chéron B G 2010 *Spectrochim. Acta* B **65** 830
[32] Kentzer C P 1986 *AIAA J.* **24** 691
[33] Gross R A 1965 *Rev. Mod. Phys.* **37** 724
[34] Bourdon A and Vervisch P 1997 *Phys. Rev.* E **55** 4634
[35] Armenise I, Capitelli M, Colonna G and Gorse C 1996 *J. Thermophys. Heat Transfer* **10** 397
[36] Esposito F, Armenise I and Capitelli M 2006 *Chem. Phys.* **331** 1
[37] Capitelli M, Ferreira C M, Gordiets B F and Osipov A I 2000 *Plasma Kinetics in Atmospheric Gases* (Berlin: Springer)
[38] Park C 1988 *J. Thermophys.* **2** 8
[39] Lotz W 1968 *Z. Phys.* **216** 241
[40] Teulet P, Sarrette J-P and Gomes A-M 1999 *J. Quant. Spectrosc. Radiat. Transfer* **62** 549
[41] Bultel A, Chéron B G, Bourdon A, Motapon O and Schneider I F 2006 *Phys. Plasmas* **13** 043502
[42] Starik A M, Titova N S and Arsentiev I V 2010 *Plasma Sources Sci. Technol.* **19** 015007
[43] Kossyi I A, Kostinsky A Yu, Matveyev A A and Silakov V P 1992 *Plasma Sources Sci. Technol.* **1** 207
[44] Kim Y K and Desclaux J P 2002 *Phys. Rev.* A **66** 012708
[45] Peterson J R *et al* 1998 *J. Chem. Phys.* **108** 1978
[46] Laux C O and Kruger C H 1992 *J. Quant. Spectrosc. Radiat. Transfer* **48** 9
[47] Holstein T 1947 *Phys. Rev.* **72** 1212
[48] Cauchon D L 1972 *Radiative Heating Results from the FIRE II Flight Experiment at a Reentry Velocity of 11.4 Kilometers per Second* NASA TM-X-1402
[49] Matsuda A, Fujita K, Shunichi S and Abe T 2004 *J. Thermophys. Heat Transfer* **18** 342
[50] Johnston C O 2006 *Nonequilibrium Shock-Layer Radiative Heating for Earth and Titan Entries* (Blacksburg, VA: Virginia State University)
[51] Cornette E S 1966 *Forebody Temperatures and Calorimeter Heating Rates Measured during Project FIRE II Reentry at 11.35 Kilometers per Second* NASA TM-X-1305
[52] Panesi M, Magin T, Bourdon A, Bultel A and Chazot O 2009 *J. Thermophys. Heat Transfer* **23** 236
[53] Panesi M, Magin T, Bourdon A, Bultel A and Chazot O 2011 *J. Thermophys. Heat Transfer* **25** 361
[54] Bultel A, Annaloro J, Morel V and Omaly P 2012 *ESCAMPIG 2012 (Viana do Castelo, Portugal)* p 325
[55] White T, Cozmuta I, Sanstos J A, Laub B and Mahzari M 2011 *42nd AIAA Thermophysics Conf. (Honolulu, HI)* AIAA 2011-3957 p 1
[56] Rond C, Boubert P, Félio J-M and Chikhaoui A 2007 *Chem. Phys.* **340** 93
[57] Rond C, Bultel A, Boubert P and Chéron B G 2008 *Chem. Phys.* **354** 16
[58] Lequang D, Babou Y, Bultel A and Marraffa L 2011 *7th European Symp. on Aerothermodynamics (Bruges)*
[59] Boubert P, Bultel A, Chéron B G and Vervisch P 2009 *J. Tech. Phys.* **50** 163
[60] Koch B-P, Goepp N and Bruhn B 1997 *Phys. Rev.* E **56** 2118
[61] Rini P, Vanden Abeele D and Degrez G 2006 *J. Thermophys. Heat Transfer* **20** 31
[62] Sanchez A L, Balakrishnan G, Linan A and Williams F A 1996 *Combust. Flame* **105** 569
[63] Pai S I 1954 *Fluid Dynamics of Jets* (New York: Van Nostrand)
[64] Bykova N G and Kuznetsova L A 2004 *Plasma Phys. Rep.* **30** 962
[65] Rini P, Vanden Abeele D and Degrez G 2007 *J. Thermophys. Heat Transfer* **21** 28
[66] Surzhikov S T 2008 *Electronic Excitation in Air and Carbon Dioxide Gas* (*VKI Lecture Series*) RTO-EN-AVT-162
[67] Park C 2008 *AIAA Paper* 2008-1446 1
[68] Zalogin G N, Kozlov P V, Kuznetsova L A, Losev S A, Makarov V N, Romanenko Yu V and Surzhikov S T 2001 *Tech. Phys.* **46** 10
[69] Reisler H, Mangir M S and Wittig C 1980 *J. Chem. Phys.* **73** 2280
[70] Mangir M S, Reisler H and Wittig C 1980 *J. Chem. Phys.* **73** 829
[71] Baughcum S L and Oldenborg R C 1984 *ACS Symp. Ser.* **249** 257
[72] Becker K H, Donner B, Freitas Dinis C M, Geiger H, Scmidt F and Wiesen P 2000 *Z. Phys. Chem.* **214** 503

[73] Bauer W, Becker K H, Bielefeld M and Meuser R *Chem. Phys. Lett.* **123** 33
[74] Smith G P *et al* www.me.berkeley.edu/gri_mech/
[75] Gorse C, Cacciatore M and Capitelli M 1984 *Chem. Phys.* **85** 165
[76] Aliat A 2008 *Physica* A **387** 4163
[77] Losev S A and Shatalov O P 1990 *Sov. J. Chem. Phys.* **6** 3299
[78] Brunger M J and Buckman S J 2002 *Phys. Rep.* **357** 215
[79] Beck W H and Mackie J C 1975 *J. Chem. Soc.: Faraday Trans.* I **71** 1975
[80] Hirschfelder J O, Curtis C F and Byron Bird R 1954 *Molecular Theory of Gases and Liquids* (New York: Wiley)
[81] Neufeld P D, Janzen A R and Aziz R A 1972 *J. Chem. Phys.* **57** 1100
[82] Vissers G W M, Heßelman A, Jansen G, Wormer P E S, van der Avoird A 2005 *J. Chem. Phys.* **122** 054306
[83] Babou Y 2007 *Transferts Radiatifs dans les Plasmas de Mélanges CO_2-N_2 : Base de Données Expérimentale et Application aux Rentrées Atmosphériques* (Orsay: Université de Paris-Sud)
[84] Kirby K and Cooper D L 1989 *J. Chem. Phys.* **90** 4895
[85] da Silva M L 2004 *Simulation des Propriétés Radiatives du Plasma entourant un Véhicule traversant une Atmosphère Planétaire à Vitesse Hypersonique* (Orléans: Université d'Orléans)
[86] Sumi T, Fujita K, Kurotaki T, Ito T, Mizuno M and Ishida K 2005 *Trans. Japan Soc. Aero. Space Sci.* **48** 40